



# Implicit method and slope limiter in AHMR procedure for high order discontinuous Galerkin methods for compressible flows

Éric Schall, Nicolas Chauchat

## ► To cite this version:

Éric Schall, Nicolas Chauchat. Implicit method and slope limiter in AHMR procedure for high order discontinuous Galerkin methods for compressible flows. Communications in Nonlinear Science and Numerical Simulation, 2019, 72, pp.371-391. 10.1016/j.cnsns.2018.12.020 . hal-02132409

HAL Id: hal-02132409

<https://univ-pau.hal.science/hal-02132409>

Submitted on 17 May 2019

**HAL** is a multi-disciplinary open access archive for the deposit and dissemination of scientific research documents, whether they are published or not. The documents may come from teaching and research institutions in France or abroad, or from public or private research centers.

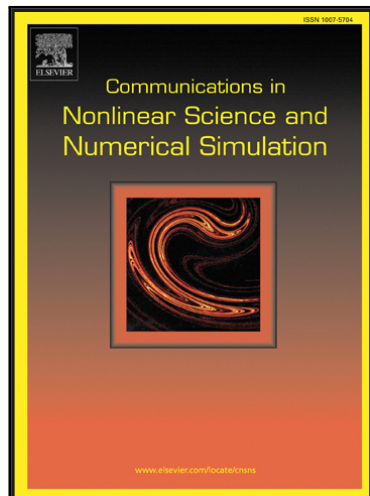
L'archive ouverte pluridisciplinaire **HAL**, est destinée au dépôt et à la diffusion de documents scientifiques de niveau recherche, publiés ou non, émanant des établissements d'enseignement et de recherche français ou étrangers, des laboratoires publics ou privés.

# Accepted Manuscript

Implicit method and slope limiter in AHMR procedure for high order discontinuous Galerkin methods for compressible flows

Eric Schall, Nicolas Chauchat

PII: S1007-5704(18)30402-7  
DOI: <https://doi.org/10.1016/j.cnsns.2018.12.020>  
Reference: CNSNS 4722



To appear in: *Communications in Nonlinear Science and Numerical Simulation*

Received date: 31 January 2018  
Revised date: 25 December 2018  
Accepted date: 27 December 2018

Please cite this article as: Eric Schall, Nicolas Chauchat, Implicit method and slope limiter in AHMR procedure for high order discontinuous Galerkin methods for compressible flows, *Communications in Nonlinear Science and Numerical Simulation* (2018), doi: <https://doi.org/10.1016/j.cnsns.2018.12.020>

This is a PDF file of an unedited manuscript that has been accepted for publication. As a service to our customers we are providing this early version of the manuscript. The manuscript will undergo copyediting, typesetting, and review of the resulting proof before it is published in its final form. Please note that during the production process errors may be discovered which could affect the content, and all legal disclaimers that apply to the journal pertain.

# Implicit method and slope limiter in AHMR procedure for high order discontinuous Galerkin methods for compressible flows

ERIC SCHALL\* AND NICOLAS CHAUCHAT

UNIV PAU & PAYS ADOUR/E2S UPPA, LABORATOIRE DES SCIENCES DE L'INGENIEUR

APPLIQUEES A LA MECANIQUE ET AU GENIE ELECTRQUE - IPRA, EA4581, 64000, PAU, FRANCE

[eric.schall@univ-pau.fr](mailto:eric.schall@univ-pau.fr)

## Abstract

In this paper the robustness and the performance of adaptive hierarchical mesh refinement (AHMR) for high order Discontinuous Galerkin (DG) finite element method with slope limiting procedure combined with an implicit time scheme for the 2D non-linear Euler equations are shown. A slope limiting procedure based on triangular meshes is implemented and has been extended and amended accordingly to suit quadrilateral elements. The combination of DG methods and slope limiters is generally used with explicit time schemes. Here, the slope limiter implemented is incorporated into a quasi implicit time scheme procedure combined with an automatic *h-adaptive* hierarchical mesh refinement allowing non-conforming meshes. The time scheme is the implicit Second Order Backward Difference Formula (BDF2) with varying time step. The numerical test cases including subsonic, transsonic and supersonic flows show that the current slope limiting with quadrilateral meshes process together with the implicit time scheme is able to remove overshoots and undershoots around high gradient regions while preserving the high accuracy of the DG method. While combining this procedure with the automatic *h-adaptive* mesh refinement, one can improve the accuracy of the solutions and be able to capture quite precisely the features of the flows under consideration. The AHMR automatic procedure presented can easily be implemented in the numerical resolution of any physical models. Furthermore the limiting method used in this paper can be generalized to any type of mesh in two dimensions.

**KEY WORDS:** Non-linear Euler equations, Discontinuous Galerkin finite elements methods (DG-FEM), Implicit time scheme, Slope limiter, Adaptive hierarchical mesh refinement (AHMR), hierarchical and non-hierarchical meshes, non-conforming meshes, *a posteriori* error estimate, wall boundary condition with curvature.

---

\*Corresponding author

## 1 Introduction

Significant efforts have been made in the development of the discontinuous Galerkin finite element methods (DGFEM) for fluid flow and heat transfer applications. The DGFEM method has been successfully used to solve non-linear hyperbolic systems of conservation laws [2, 9]. Since it uses discontinuous piecewise polynomial bases, the discretization is locally conservative, and, in the considered lowest-order case, the method preserves the maximum principle for scalar equations.

Nevertheless, for high order schemes, around sharp gradients and discontinuities, if the solution does not remain smooth for a long period of time, there occurs oscillations commonly called Gibbs phenomenon. Many studies in literature deal with this subject [9, 14, 7]. These oscillations due to discontinuities, are sometimes severe to cause stability problem [9, 22]. There are two strategies applied to deal with this situation. A shock-capturing method [1] or an appropriate slope limiter is commonly used to suppress these oscillations while preserving the high order accuracy in smooth regions [20]. For low approximation order (and polynomial degrees  $p < 3$ ), the slope limiting procedure remains the alternative for shock capturing [14]. In [7], Cockburn argued that the slope limiter is equivalent to a nonlinear form of artificial viscosity. The slope limiter proposed use the same technical approach as the one used in Tu et al [22] for DG methods. This limiter is differentiable [13] and used the area-weighted based formula [10, 22] to compute the gradient. Generally slope limiters are implemented in DG methods combined with explicit time schemes such as Runge-Kutta methods. The reason of not using implicit time scheme is that the slope limiters are non-differentiable [23]. A way of incorporating the slope limiter into an implicit time scheme (BDF2) procedure is proposed with varying time step by introducing a residual based on the limited solution. By so doing one can use a relatively coarse mesh with no restriction of the CFL to obtain an accurate solution in comparison to an explicit scheme.

Another aspect tackled is the combination of the proposed slope limiter incorporated into an implicit time scheme with an automatic *h-adaptive* mesh refinement (AHMR) with hanging-nodes designed in our DG methods library **Concha**, on both quadrilateral and triangular meshes. The adaptive mesh refinement is

based on *a posteriori* error estimator using the jump at interface of physical quantity such as density. The strategy of the AHMR is to iteratively improve the quality of the approximate solutions at high order based on computed information (*a posteriori* error analysis). In this way, a sequence of locally refined meshes is constructed, which allows better efficiency compared to classical approaches in the presence of different kind of singularities. Thus by combining the AHMR with an implicit time scheme with a high order DG method, one can use a relatively coarse mesh with few number of adaptive refinement to obtain accurate solutions in a very reasonable computational time.

The organization of this paper is as follows: section 2 describes the governing equations and the spatial discretization, implementation of numerical fluxes schemes, and the time discretion scheme procedure. Section 3 describes the implicit BDF2 time integration with varying time step scheme and the strategy of incorporating the slope limiter into the implicit time scheme procedure. Section 4 describes succinctly the limiting procedure on both triangular and quadrilateral meshes. In section 6, the Adaptive mesh refinement (AHMR) is described. In section 7 five numerical test cases are considered ranging from subsonic to supersonic flows to show :

- the performance of the combined implicit time scheme - slope limiter in comparison with explicit Runge-Kutta scheme at high order,
- the well behaving of the combine implicit time scheme - slope limiter with subsonic and transonic flows,
- comparison of the adaptive mesh refinement with the slope limiting procedure for triangular and quadrilateral meshes.

## 2 Governing Equations and DG discretizations

### 2.1 Governing equations

The Euler equations which govern two-dimensional unsteady compressible inviscid flow can be written in the following conservative form,

$$\frac{\partial u}{\partial t} + \frac{\partial F(u)}{\partial x_i} = 0 \quad \text{in } \Omega_T = \Omega \times (0, T) \quad (2.1)$$

where  $u$  is the vector of conserved variables and  $F = (f_1, f_2)$ .  $f_1$  and  $f_2$  are the total flux vectors in the  $x_i = (x, y)$  direction respectively.  $T > 0$  is the length of time interval, and  $\Omega$  is a two-dimensional bounded domain. The conservative variables  $u$  and the inviscid components of the fluxes  $F = (f_1, f_2)$  are given respectively :

$$u = \begin{bmatrix} \rho \\ \rho v_1 \\ \rho v_2 \\ \rho E \end{bmatrix}, \quad f_1 = \begin{bmatrix} \rho v_1 \\ \rho v_1 v_1 + p \\ \rho v_1 v_2 \\ \rho H v_1 \end{bmatrix}, \quad f_2 = \begin{bmatrix} \rho v_2 \\ \rho v_1 v_2 \\ \rho v_2 v_2 + p \\ \rho H v_2 \end{bmatrix} \quad (2.2)$$

where  $\rho$  is the density of the fluid,  $v_1$  and  $v_2$  are the cartesian velocity components of the flow,  $p$  is the pressure, and  $E$  is the total specific energy.  $E$  and  $H$  are defined as:

$$E = e + \frac{v_1^2 + v_2^2}{2}; \quad H = E + \frac{p}{\rho} = e + \frac{1}{2}V^2 + \frac{p}{\rho} \quad (2.3)$$

where  $e$  is the specific static internal energy. This system of equations is closed with the perfect gas equation of state given by equation (2.4):

$$p = (\gamma - 1)\rho \left( E - \frac{v_1^2 + v_2^2}{2} \right), \quad (2.4)$$

where  $\gamma$  is defined as the ratio of specific heats of the fluid ( $\gamma = 1.4$  for air).

The system of equations (2.1) represents a hyperbolic system of equations to which are applied the initial

and boundary conditions denoted by (2.5), respectively, where  $\partial\Omega$  represents the boundary of  $\Omega$ .

$$u(x, 0) = u^0(x); \quad B(u) = 0 \quad \text{on} \quad \partial\Omega \times (0, T). \quad (2.5)$$

## 2.2 Discontinuous Galerkin spatial discretization

Suppose that the computational domain  $\Omega$  is partitioned into disjoint open elements  $K$  such that  $\bar{\Omega} = \sqcup_{K \in \mathcal{T}_h} \bar{K}$ .  $h$  represents de piecewise constant mesh function defined by  $h|_K \equiv h_K = \text{diam}(K)$  for all  $K \in \mathcal{T}_h$ . The DG finite element approximations  $u_h$  and  $v_h$  are obtained using truncated polynomial expansions combined with  $m$  shape functions  $\phi_i$ , expressed as:

$$u_h = \sum_{i=1}^m u_h \phi_i(x); \quad v_h = \sum_{i=1}^m v_h \phi_i(x) \quad (2.6)$$

In this work, hierarchical shape functions are used on both triangles and quadrilaterals [6, 5, 24]. Considering possible choices of basis functions and then by multiplying by a test function  $v$  and integrating by parts, one obtains after discretization over the whole domain, the following formulation [8, 11]:

$$\sum_{K \in \mathcal{T}_h} \left\{ \int_K \frac{\partial u}{\partial t} v_h - \int_K F(\mathbf{u}_h) \cdot \nabla v_h dx + \int_{\partial K \setminus \Gamma} H(\mathbf{u}_h^+, \mathbf{u}_h^-, n) v_h^+ ds + \int_{\partial K \cap \Gamma} H(\mathbf{u}_h^+, \mathbf{u}_h^-, n) v_h^+ ds \right\} = 0 \quad (2.7)$$

where  $n = (n_x, n_y)$  is the outward to the boundary unit normal. The interfaces flux  $F(u) \cdot n$  are replaced by Riemann numerical flux functions  $H(\mathbf{u}_h^+, \mathbf{u}_h^-, n)$  at the interfaces of two adjacent cells. Let's define  $\mathbf{u}_h^+$  and  $\mathbf{u}_h^-$  as the right and the left state of  $u$ . For the interior interfaces, the well known HLLC, Roe and Vijayasundaram Riemann solvers [21, 11] are used. For the boundaries numerical flux, a robust numerical flux is implemented and expressed as follows:

- The numerical flux implemented for boundary conditions  $\mathcal{H}(\mathbf{u}_h^+, u_\Gamma(u), n)$

$$\begin{cases} \mathcal{H}(\mathbf{u}_h^+, u_\Gamma(u), n) = R(u_\Gamma(u), n) \lambda_i L(u_\Gamma(u), n) u_h^+ & \text{if } \lambda_i \geq 0 \\ \mathcal{H}(\mathbf{u}_h^+, u_\Gamma(u), n) = R(u_\Gamma(u), n) \lambda_i L(u_\Gamma(u), n) u_h^- & \text{if } \lambda_i < 0 \end{cases} \quad (2.8)$$

where  $\lambda_i$  denotes the eigenvalues of the Jacobian matrix  $\mathcal{A}(w, n) = \frac{\partial F(w)}{\partial u} \cdot n$  in the neighborhood of  $\partial K$ ,  $R(u, n)$  and  $L(u, n)$  are the right and the left eigenvectors matrix respectively.  $u_\Gamma(u) = g_D$  represents the state of  $u$  depending on the type of boundary condition applied (inflow supersonic or subsonic, outflow supersonic or subsonic, and slip wall boundary, see [11]).

### 3 Time integration : Implicit second order Backward Difference formula (BDF2) with variable time step

This section is devoted to the description of the implicit time scheme applied to the DGFEM discretization (2.7) of the problem (2.1). An adaptive time-stepping implicit two-step Backward Differentiation Formulas (BDF2) with Newton iterations is employed into which the limiter procedure has been incorporated. The system (2.7) can be written globally on the whole triangulation  $\mathcal{T}_h$  in the matrix-vector form as follows :

$$\mathcal{M} \frac{d}{dt} u_h = \mathcal{R}_h \quad (3.1)$$

where  $\mathcal{M}$  is the mass matrix of the system,  $u_h$  is the time-dependent vector of all unknowns, and  $\mathcal{R}_h$  is the vector of all the right hand sides of the equation (2.7). As already said, the explicit methods [9, 17, 22] are easy to apply but impose a time step restriction. Introducing an implicit time strategy can help avoiding small time step and allows the use of relatively coarse mesh to capture the sharp gradients and other sensitive features in the flow domain. The BDF2 scheme is coupled with Newton iteration method into which is introduced the limiting procedure to calculate the residual for updating the solution.

The BDF2 time integration scheme combined with variable time stepping reads:

$$\mathcal{M} \frac{c_2 - 1}{c_2 - c_1} u^{n+1} + \mathcal{M} \frac{c_2}{c_2 - c_1} u^n - \mathcal{M} \frac{1}{c_2 - c_1} u^{n-1} - \Delta t_n \mathcal{R}_h(u^{n+1}) = \mathcal{R}_e(u^{n+1}) \quad (3.2)$$

where  $c_1 = \frac{\Delta t_n + \Delta t_{n-1}}{\Delta t_n}$ , and  $c_2 = c_1^2$ .  $n$  is the index of the time iteration.  $\mathcal{R}_e$  denotes the unsteady-state residual.

To solve this implicit problem (3.2), for the  $n + 1$  time step, the usual Newton iteration method reads :

$$\begin{aligned} (i) \quad & w^1 = u^n \\ (ii) \quad & \left[ \frac{\partial \mathcal{R}_e}{\partial w} \right]^k \Delta w^{k+1} = -\mathcal{R}_e(w^k), \quad w^{k+1} = w^k + \alpha \Delta w^{k+1}, \quad k = 1, 2, \dots, m \\ (iii) \quad & u^{n+1} = w^m, \quad \text{when } \mathcal{R}_e(w^m) \leq \max(\eta_1, \eta_2 * \|\mathcal{R}_h^m\|_{L_\infty}) \end{aligned} \quad (3.3)$$

where  $\alpha$  is the relaxation parameter, which takes values between 0.8 and 1 according to the stiffness of the test case.  $w$  represents intermediate solutions in the Newton solver process for the solution of  $u^{n+1}$ , which is satisfied with  $\left[ \frac{\partial \mathcal{R}_e}{\partial w} \right] = \frac{\partial \mathcal{R}_e}{\partial u_h}$ .  $\eta_1$  and  $\eta_2$  are tolerance parameters fixed by the user. Generally,  $\eta_1 = 10^{-6}$  and  $\eta_2 = 10^{-12}$  are fixed arbitrary constants

Now in order to introduce the slope limiting procedure in the implicit iteration, a modification to the Newton iteration is proposed. Thus the Newton iteration coupled with the limiting procedure becomes :

$$\begin{aligned} (i) \quad & w^1 = u^n \\ (ii) \quad & \left[ \frac{\partial \mathcal{R}_e}{\partial w} \right]^k \Delta w^{k+1} = -\mathcal{R}_e(w^k), \quad w^{k+1} = w^k + \alpha \Delta w^{k+1}, \quad k = 1, 2, \dots, m \\ (iii) \quad & u^{n+1} = \mathcal{L}(w^m), \quad \text{when } \text{limiterResidual} \leq \max(\eta_1, \eta_2 * \|\mathcal{L}(w^m)\|_{L_\infty}) \end{aligned} \quad (3.4)$$

where  $\mathcal{L}$  denotes a generic limiting operator. The next section presents the slope limiting operator used in the case of limited gradients. The *limiterResidual* is computed as follows :

$$\text{limiterResidual} = \sqrt{\frac{\sum_{i=1}^{ncomp} \sum_{j=1}^{ne} (u^{limnew} - u^{limold})^2}{ncomp * ne}} \quad (3.5)$$

where  $u^{limnew}$  and  $u^{limold}$  are the limited solutions at the current time step and the previous one respectively, calculated at the center of the element;  $ncomp$  is the number of component of the conservative state vector (4 for 2D Euler equations),  $ne$  is the total number of elements. Having modified the Newton iteration combined with the limiter procedure, for convergence purpose the first residual for the iterative Newton is computed as follows :

$$Res = \frac{\sqrt{\frac{\sum_{i=1}^{ncomp} \sum_{j=1}^{ne} (u^{limnew} - u^{limold})^2}{ncomp * ne}}}{\Delta t \|u^{n+1}\|_{L_\infty}} \quad (3.6)$$

## 4 Slope limiting procedure

It may be noted that the limiting method used in this paper for triangular or quadrilateral cells can be generalized to any type of cell in two dimension. Primitive variables are used in the limiting procedure in order to apply a positivity checks after variables gradients are limited. This is to prevent solutions with locally negative density and/or pressure solution values [12, 18].

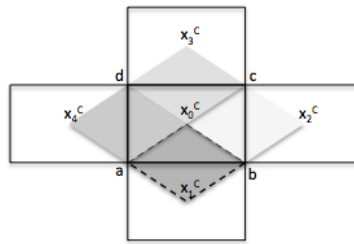


Figure 1: *Patch neighborhood used for the limiting algorithm.*

After computing the unlimited gradient of the primitive variables on the current cell and its neighbours according to the area-weighted formula [22], following the patch in Figure 1, the limited gradient can be written in its generalized form as :

$$(\nabla V_0)^l \approx \sum_{i=1}^n w_i (\nabla V)_i \quad (4.1)$$

where  $n$  is the number of segments per element. The weights in their generalized form read :

$$w_i = \frac{\prod_{j \neq i}^n g_j + \epsilon}{\sum_{j=1}^n g_j^2 + n\epsilon} \quad (4.2)$$

with  $\epsilon$  set to  $10^{-10}$  used to avoid division by zero and  $g_j$  is chosen as the square of the  $L_2$  norm of the unlimited element gradients, i.e.  $g_i = \|(\nabla V)_i\|^2$ .

Then the product rule is used to reconstruct the gradients of the conservative variables and then evaluate the first order accurate three-term Taylor expansion of the conservative variables while preserving the cell

averages of the unlimited conserved variables.

$$V^l = \bar{V}_0 + \begin{pmatrix} dx \\ dy \end{pmatrix} \cdot (\nabla V_0)^l |_{(x_0, y_0)} \quad (4.3)$$

where

$$\bar{V}_0 = \frac{1}{|K|} \int_K V dx; \quad dx = x - \frac{1}{|K|} \int_K x dx; \quad dy = y - \frac{1}{|K|} \int_K y dy. \quad (4.4)$$

Due to the presence of high gradients, rarefaction zones and impulsive initial conditions, negative values of density and pressure can occur during the time integration process, mainly at the initial stages. To avoid the appearance of local spurious negative density and pressure values of the thermodynamic variables  $\rho$  and  $p$  during the iterative process, density and pressure are updated, if necessary, using some kind of relaxation (see equation 4.5). This must assure that they are always positive. For instance, pressure update is modified according to equation :

$$p^{n+1} = p^n + \Delta p \left[ 1 + \eta \left( \alpha + \left| \frac{\Delta p}{p^n} \right| \right) \right]^{-1} \quad (4.5)$$

whenever  $\frac{\Delta p}{p^n} \leq \alpha$ , where  $\eta = 2$  and  $\alpha = -0.2$ . Similar procedure is used for the density (see [18] for more details).

## 5 Boundary treatment for curved edges

As pointed out by many authors it is important, for DG methods, to modify the discretization scheme for high order at curved boundaries in order to avoid oscillations in the solution and spurious entropy production [3, 19, 15]. To have an accurate approximation of geometric boundaries, for adjacent elements to curved boundaries as the solid walls, the standard linear parametrization is replaced by a polynomial representation with respect to the analytical description of the boundary on a simplex element of higher order. In the transformation from a reference element to the curved element (Figure 2), the concerned edge is expressed in terms of Lagrange polynomials and is calculated from additional points on the curved boundary [3, 19]. So, during the refinement process, more grid points are inserted on the solid wall in order

to take into account the curvature of the geometric boundaries.

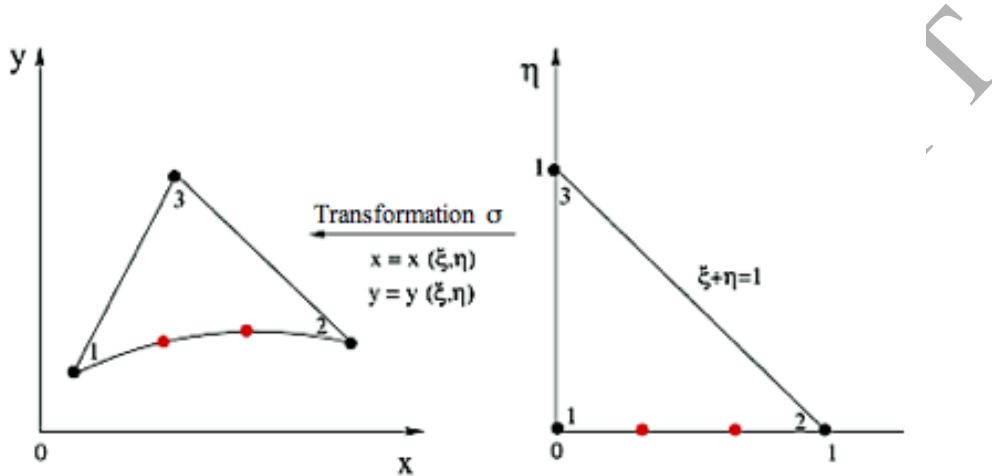


Figure 2: Geometric transformation to a cell with curved edge.

## 6 Adaptive mesh refinement procedure

The adaptive mesh refinement strategy adopted here is classical (see [5] or [16]). Briefly, the standard refinement procedure reads: starting from an initial mesh, after a quasi-converged solution and accuracy, the cells are marked according to different tolerance levels for the error indicator. Then the new grid is obtained and calculation can go on. A full description of the present procedure with the necessary parameters can be found in [5]. The typical structure of this adaptive algorithm is the following :

$$\text{Solve} \rightarrow \text{Estimate} \rightarrow \text{Mark} \rightarrow \text{Refine.} \quad (6.1)$$

For implicit calculations during the refinement procedure, the non-linear and the stationary residuals (see equation (3.5)) must drop to  $10^{-4}$  for any given mesh.

## 7 Numerical experiments

Numerical results are presented with the implicit time scheme combined with the limiting procedure to show the robustness and the accuracy of the solutions for 5 test cases ranging from subsonic to supersonic flows : Shock-tube, NACA0012, Ramp, Cylinder and Scramjet. The last two cases will be run with the adaptive mesh refinement procedure (AHMR) on both triangular and quadrilateral mesh for comparison. Through these numerical experiments particular attention is paid to some relevant aspects of numerical simulations such as :

- spacial interpolation, comparing the accuracy of the DG scheme at high order when using the slope limiter (all the test cases),
- time integration, comparing the explicit and the implicit schemes in term of precision and mesh resolution ( Shock-tube and Ramp test cases),
- robustness of the slope limiter, testing the slope limiter for transsonic flow with various shock waves magnitudes (NACA0012 test case),
- geometry type of mesh, comparing the solutions obtained while dealing with quadrangular and triangular type of mesh in an adaptive mesh refinement (AHMR) procedure (Cylinder and Scramjet test cases). The AHMR process combined with high order schemes with limiting procedure give good results in capturing the discontinuities and others sensitive features of the flow in the computational domains. However, some significant differences appear depending on the type of mesh in comparing results on triangular and quadrangular meshes.

Table 1 represents the various test cases considered and the panel of calculations performed with them.

Test Case / Num. Method.	Explicit	Implicit	Quad.	Tri.	DG0	DG1	Physical
Shock Tube	X	X	X	X	X	Limited & not limited	Quasi 1D / Transient flow
Ramp	X	X	X		X	Limited & not limited	2D / Supersonic external flow
Naca		X		X		Limited	2D / Transsonic external flow
Cylinder+AHMR		X	X	X	X	Limited	Supersonic external flow
Scramjet+AHMR		X	X	X	X	Limited	Supersonic internal flow

Table 1: *Description of the numerical experiments. Test cases on the first left column and numerical methods on the first line.*

(*quad*) and (*tri*) stand for quadrangular or triangular mesh respectively.

## 7.1 Shock tube

Simulation of the shock tube problem is adopted to validate the behavior of the limiting procedure with an analytic solution. Through a thin tube, 2D simulation of this 1D problem (see equations 7.1-7.3) is performed using the limiter implemented. The computational is 10 meters long and 1 meter thick.

$$\rho(x, 0) = \begin{cases} 1.0 & \text{for } x \leq 0 \\ 0.125 & \text{for } x > 0 \end{cases}, \quad (7.1)$$

$$p(x, 0) = \begin{cases} 1.0 & \text{for } x \leq 0 \\ 0.1 & \text{for } x > 0 \end{cases}, \quad (7.2)$$

$$u(x, 0) = 0. \quad (7.3)$$

The HLLC Riemann solver is used. The mesh used is displayed in Figure 3 and contains 2400 cells. The Computed and analytical solutions are given at  $t = 1.s$ . The computed density distributions are shown in Figures(4 to 6). Looking at figure 4 explicit and implicit DG1 evolutions are overlapped. Note that regarding computational efficiency, implicit is more than twenty as fast as explicit. Figure 5 shows that the limiter suppress very well the numerical oscillations including numerical diffusion in the non-limited DG1 solution. In figure 6 the DG0 solution is slightly more diffusive compared to the DG1 limited solution. Globally good agreement between the analytical solution and the computed one with the high order DG scheme using limiter is observed.

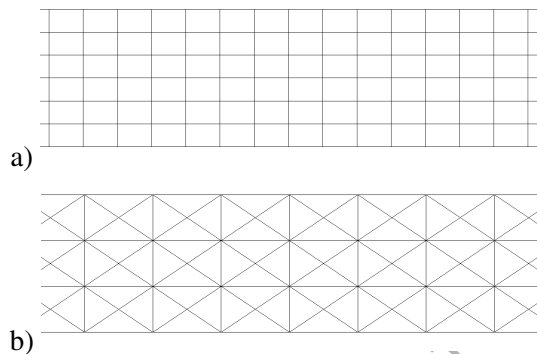


Figure 3: *Zoom in the middle of the thin tube for : (a) Quadrilateral mesh, (b) Triangular mesh, both with 2400 cells*

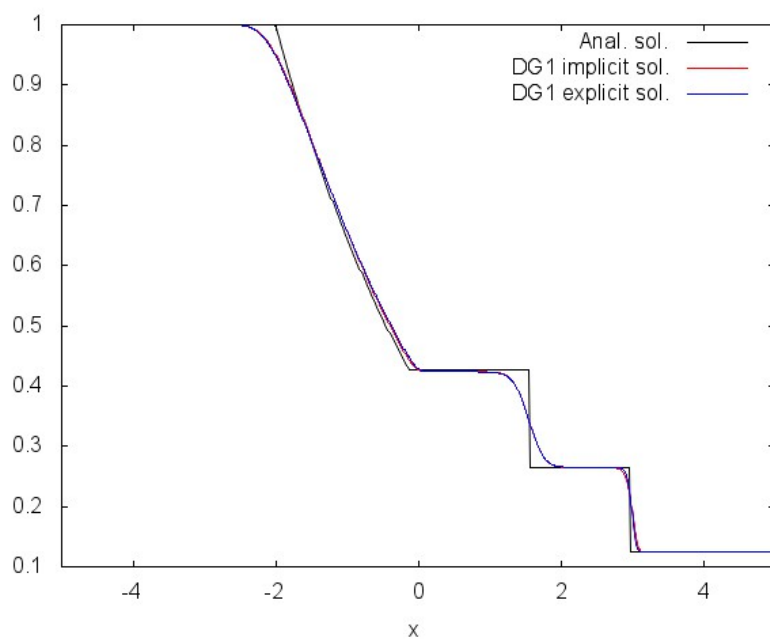


Figure 4: *Density evolution. Comparison with both Implicit and Explicit.*

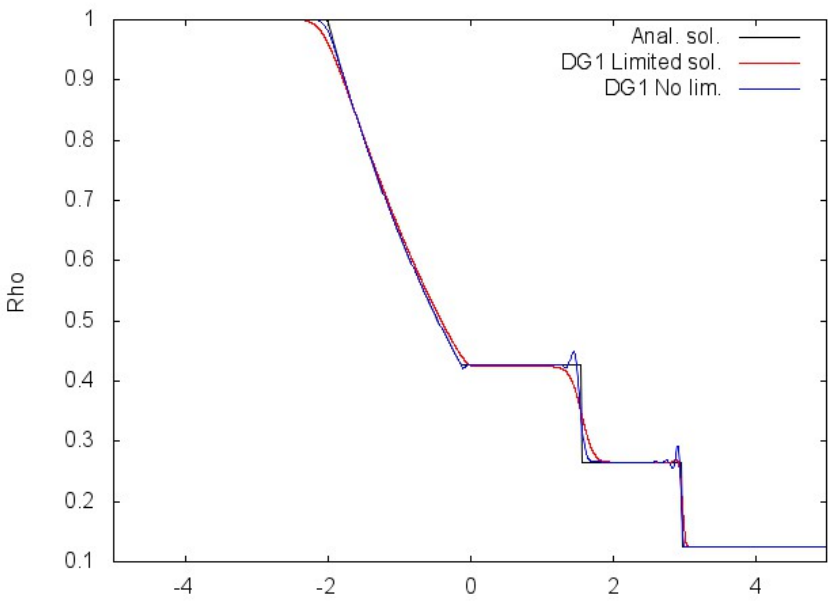


Figure 5: Density evolution. Comparison with and without any limiter.

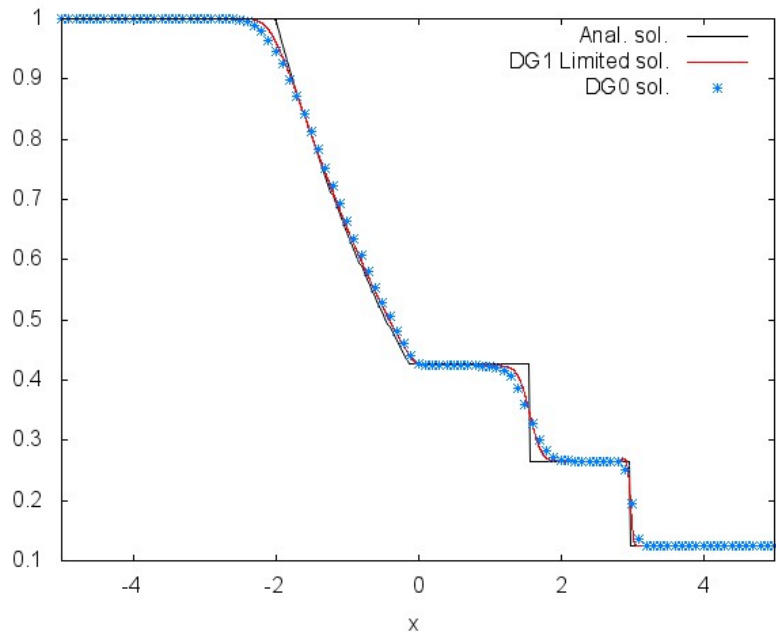


Figure 6: Density evolution. Comparison between DG0 and DG1 limited.

## 7.2 Supersonic inviscid flow passing a ramp

This case is about supersonic flow at Mach number 2 passing a ramp with  $10^\circ$  slope. The steady-state solution contains an oblique shock. A structured mesh is used consisting of only 384 quadrilaterals. Figure 7 shows the mesh (left picture) and the pressure contours at the steady state (right picture). Figure 8 shows the density cutline distributions at  $y = 0.2$  for both limited and non-limited solutions. One can observe that the numerical oscillations are suppressed and the oblique shock has been well captured. No overshoots or undershoots appear around regions with high gradients. The convergence history of the proposed limiting process is shown in Figure 9. One can notice that the mesh is relatively coarse but the limited procedure combined with the variable time step BDF2 implicit scheme is able to resolve the shock. With this implicit scheme the time step at the beginning of the calculation is  $\Delta t = 5 \cdot 10^{-4} s$  and the overall residual in time drops to  $10^{-6}$  after 25 iterations. The time step is allowed to increase during the calculation and it reached  $10^{-2}$  before convergence is achieved. Computing the case with RKDG explicit time scheme (see [17]), the time step must remain constant and is  $\Delta t = 5 \cdot 10^{-5} s$ . So to reach the same final time 1860 iterations are required with the RKDG scheme. This shows clearly the importance of the implicit method incorporated into the slope limiting procedure for high order DG in terms of computational time saving. The figure (10) shows the comparison of the implicit and the RKDG schemes solutions by realizing a cutline on the density distributions at  $y = 0.2$ . One can notice with the same mesh, the implicit scheme captured more accurately the oblique shock than the RKDG scheme.

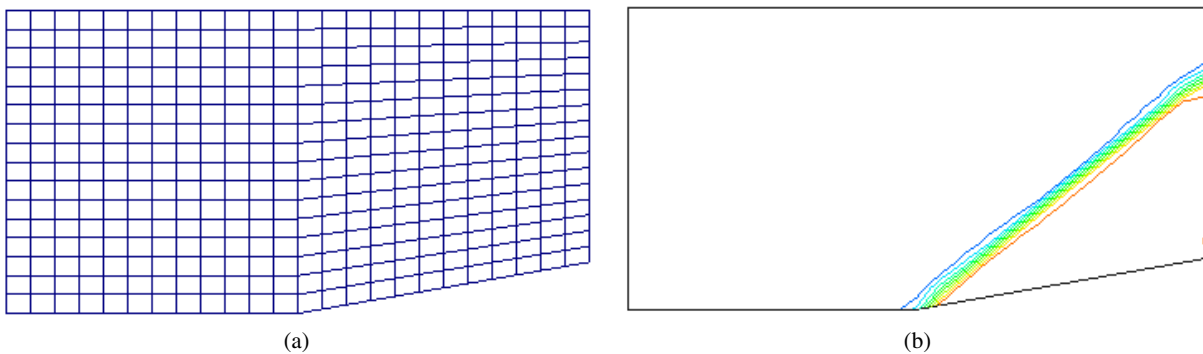


Figure 7: Supersonic flow ( $Mach = 2$ ) passing a  $10^\circ$  ramp. Left: mesh containing 384 quadrilaterals; right: pressure contours.

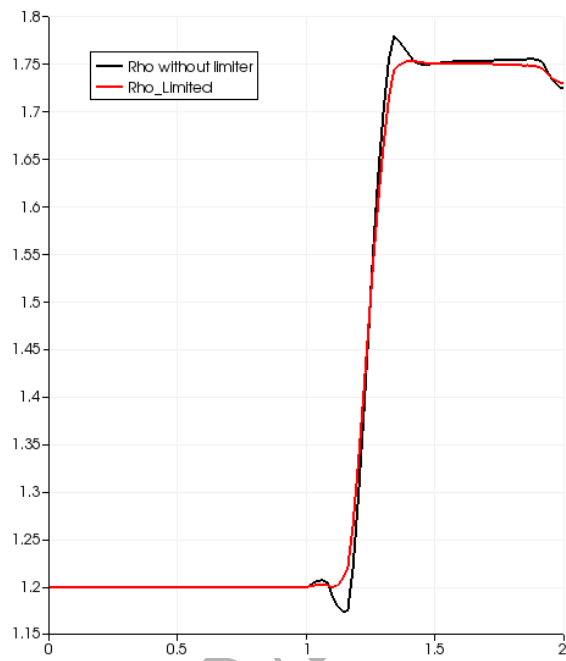


Figure 8: Density distributions (cutline at  $y = 0.2$ ): comparison between the non-limited solution and the limited solution on quadrangular mesh.

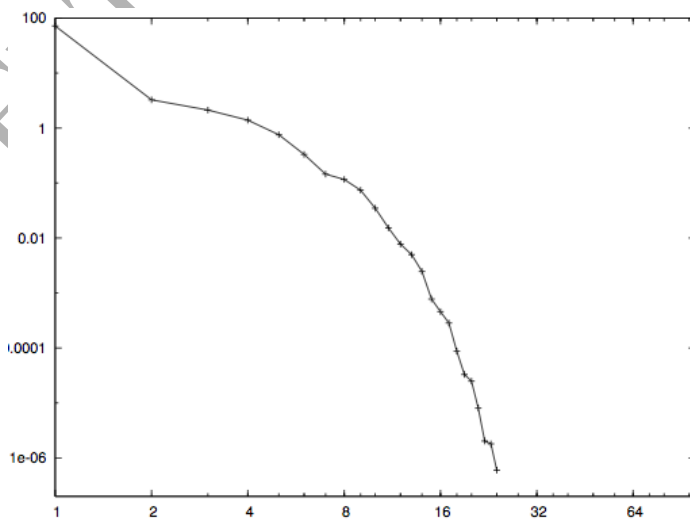


Figure 9: Supersonic flow ( $Mach = 2$ ) passing a  $10^\circ$  ramp : convergence history.

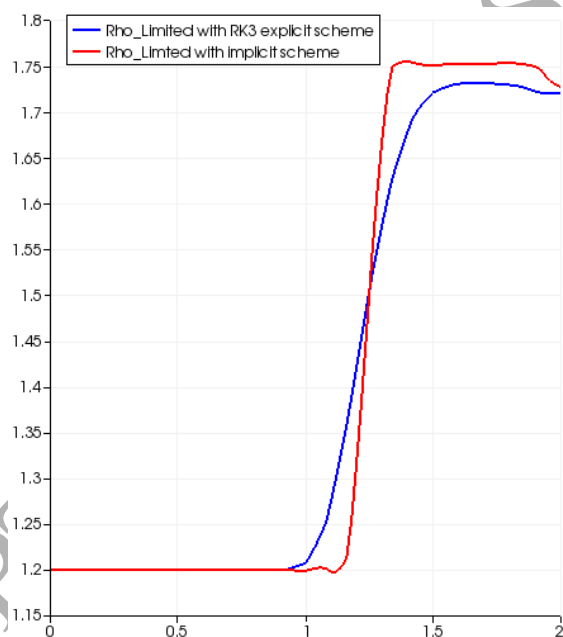


Figure 10: *Density distributions (cutline at  $y = 0.2$ ): comparison between RKDG and BDF2 scheme solutions.*

### 7.3 Transsonic flow past a NACA0012 airfoil

The third case focuses on the transsonic flow around NACA0012 airfoil. This case is about a flow at Mach number 0.85 around the NACA0012 airfoil with an angle of attack of  $1^\circ$ . Due to the acceleration of the subsonic flow on the intrados and the extrados, the flow will reach a supersonic state on part of the surface. Hence, supersonic regions will be pocketed in a subsonic region, making the overall flow transsonic. This test case is to demonstrate the impact and the accuracy of the slope limiter for flows at various shock waves magnitudes.

The computational domain shown in Figure 11 is about 40 chord lengths away from the airfoil. The mesh consists of 7195 triangular cells. Figure 12 shows the entropy distribution around the solid body using DG0 and DG1 discretization schemes. One can observe that the higher order scheme DG1 provides low dissipation away from the shock around the body. Figures 13 and 14 show the unlimited and limited pressure and Mach number contours near the airfoil surface. As it can clearly be seen, two shocks appear on the surface. The shock on the upper surface is stronger and located at a more down-stream place than the shock on the lower surface due to the angle of attack. The numerical oscillations due to high order scheme observed on the unlimited pressure and Mach number contour have been removed by the limiter without deteriorating the subsonic flow around the shock waves. The accuracy of the isolines depends on the mesh density. The pressure coefficient  $C_p$  shown in Figure 15 (left) compares the current DG1's limited solution to the DG1 non-limited and DG0 solutions. One can see that the DG1 limited solution well fitted the unlimited solution without the oscillations. The figure 15 (right), is in comparison of the current DG1 limited solution with the one from Tu & al. [22]. Good agreement can be seen in terms of the location and strength of shocks.

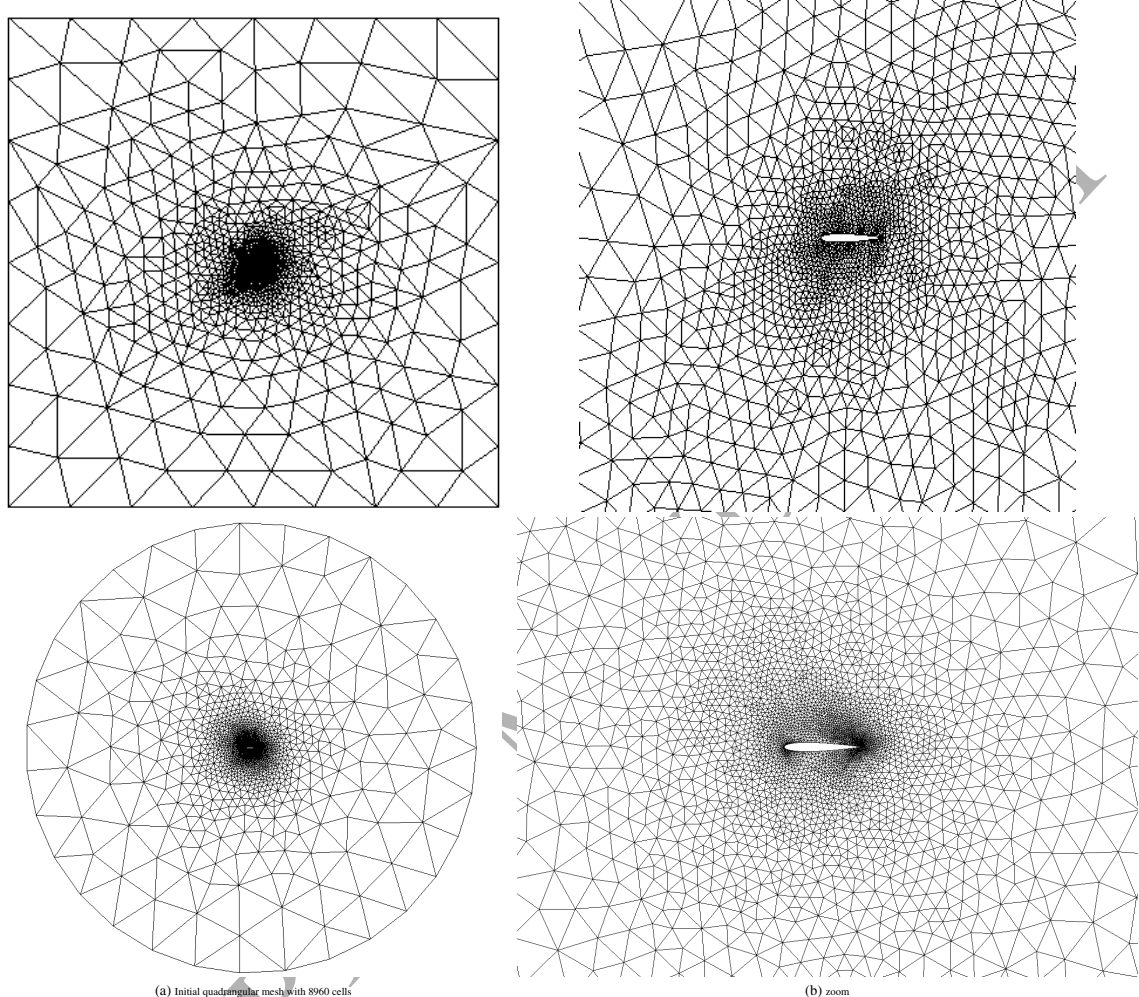


Figure 11: Mesh around NACA0012 airfoil. Left: whole; right: zoom near the airfoil.

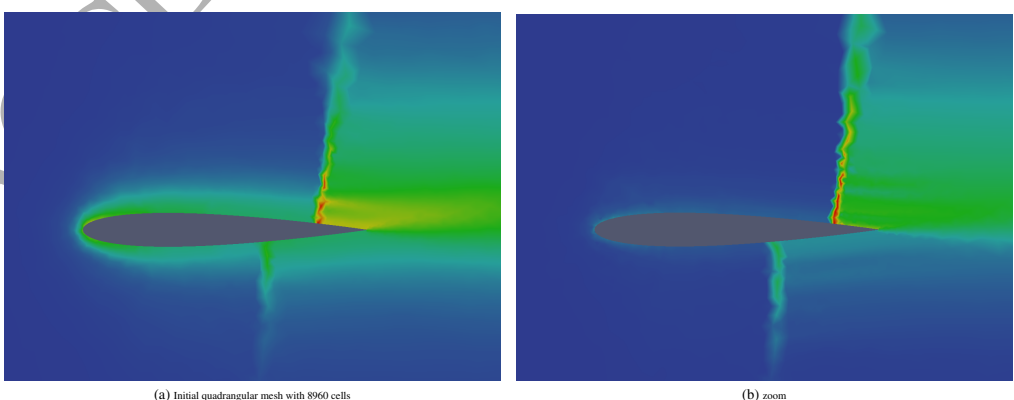


Figure 12: Entropy distribution around the NACA0012 body. Left: DG0 result; right: DG1 limited result.

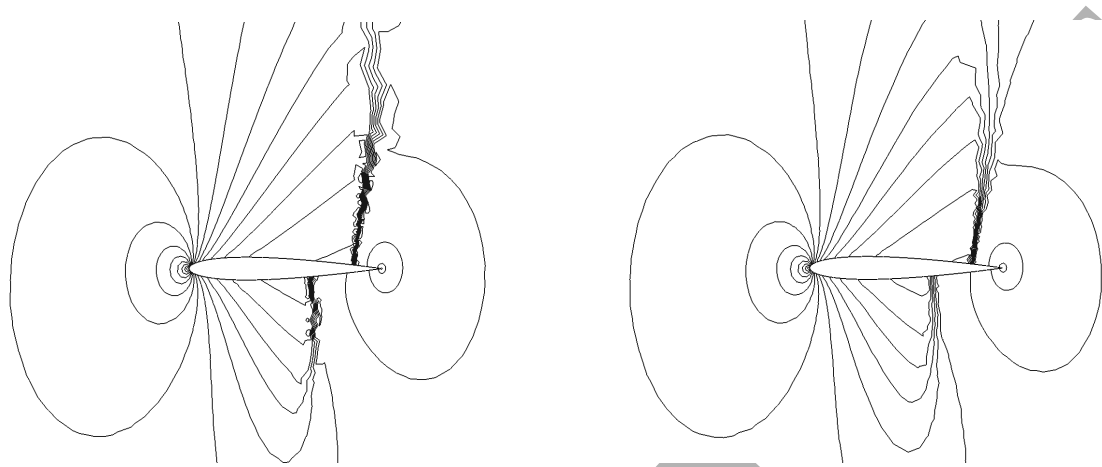


Figure 13: *Flow past a NACA airfoil test case ( $Mach = 0.85$ , angle of attack  $\alpha = 1.^\circ$ ). Left : Unlimited pressure contours; right : Limited Pressure contours.*



Figure 14: *Flow past a NACA airfoil test case ( $Mach = 0.85$ , angle of attack  $\alpha = 1.^\circ$ ). Left : Unlimited Mach number contours; right : Limited Mach number contours.*

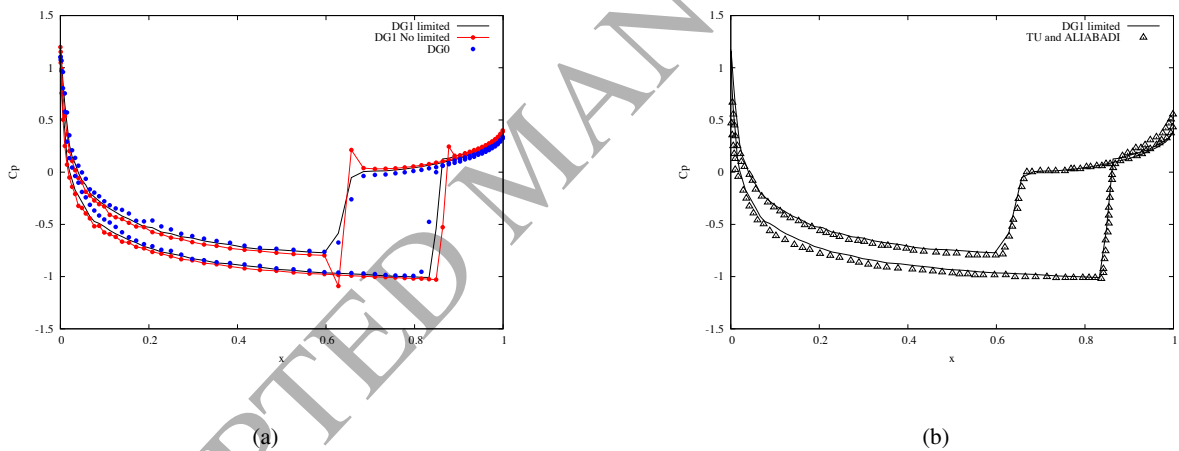


Figure 15: Flow past a NACA airfoil test case ( $Mach = 0.85$ , angle of attack  $\alpha = 1.^\circ$ ). Pressure coefficient distribution  $C_p$ . Left : Present results. Right: Comparison with others authors.

#### 7.4 Supersonic external flow past a Cylinder with AHMR procedure

This test case consists of a steady flow past a circular cylinder, at a free stream Mach number of 3 [4]. The presence of shocks, stagnation, rarefaction and vortex zones, as antagonist phenomena make this problem challenging in terms of stability behavior. So the choice of the physical criterion to minimize the local error is crucial in the adaptive mesh procedure. The error indicator is chosen to be the jump (between two cells) in Mach number. To show the robustness and the accuracy of the method the Riemann solver HLL flux is chosen which is rather diffusive.

Triangular and quadrangular meshes with DG0 and DG1 schemes have been successively investigated and evaluated. Figures 16 show initial meshes of both type of cells. The curved edges treatment's accuracy is evaluated on the solid boundary during the mesh refinement procedure with the limiter. In order to test the AHMR behavior, two different strategies are used : a coarse triangular mesh and a fine quadrilateral mesh are considered.

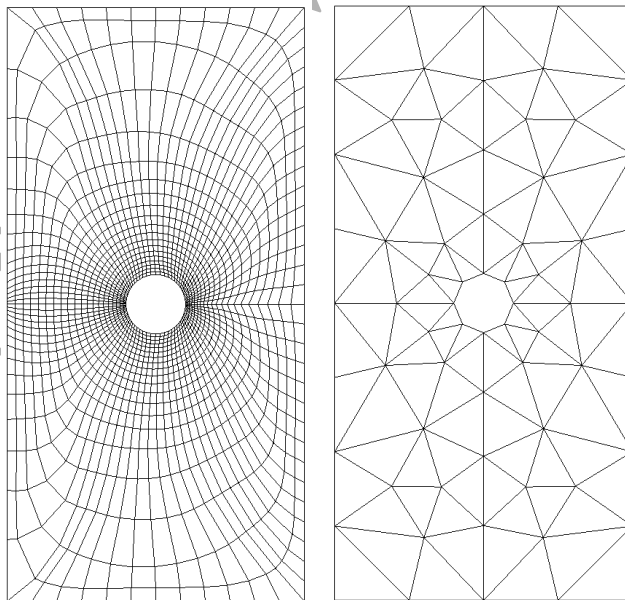


Figure 16: *Initial meshes for the cylinder test case. Left : Quadrilateral mesh with 1680 cells; right : Triangular mesh with 104 cells.*

#### 7.4.1 AHMR procedure on triangular meshes: Cylinder test case

The starting mesh named Mesh0 containing only 104 cells is chosen very coarsely with only eight segments (or straight-lines) as boundary edges to demonstrate at the same time the robustness of the adaptive method and the treatment of curved edges on solid wall boundary. Detailed mesh evolution of the AHMR is shown in Table 2 for DG0 and DG1.

Table 2: Successive adaptive meshes - Cylinder test case

<b>DG0</b>	<b>Mesh0</b>	<b>Mesh1</b>	<b>Mesh2</b>	<b>Mesh3</b>	<b>Mesh4</b>	<b>Mesh5</b>	<b>Mesh6</b>	<b>Mesh7</b>
Cells	104	242	539	1190	2480	5783	13889	27758
Points	68	161	330	711	1438	3323	7895	15400
<b>DG1</b>	<b>Mesh0</b>	<b>Mesh1</b>	<b>Mesh2</b>	<b>Mesh3</b>	<b>Mesh4</b>	<b>Mesh5</b>	<b>Mesh6</b>	
Cells	104	236	485	1100	2228	5213	12128	
Points	68	159	293	659	1299	3005	6881	

Triangular meshes with DG0 and DG1.

In Figure (d) the red polygon is the initial mesh with the straight-lines. One can see that during the refinement process, the boundary curve is well resolved in fitting the curvature of the cylinder. The streamlines at the rear of the cylinder is the seat of a rarefaction zone with vortexes in Figure 17. These vortexes are captured respectively during the sixth and the seventh level of refinement for DG1 and DG0. Figures 18 show the Mach number contour distribution on the local adaptive refined mesh for DG1 and DG0 at level six (mesh6) and seven (mesh7) respectively. The corresponding cells difference between the sixth and seventh level of refinement with DG0 discretization is shown in Figure 19. This picture shows the refined zones between two levels of the adaptive refinement procedure and can give an idea of the place where the error criterion is the most sensitive. This appreciation is very important to capture the main flow features all over the domain. The Figure 19 can be seen as the cells number that the DG0 calculation needed to add more to get a solution as accurate as the one with DG1. Nevertheless, considering the number of unknowns to solve both numerical experiences, DG1 has more.

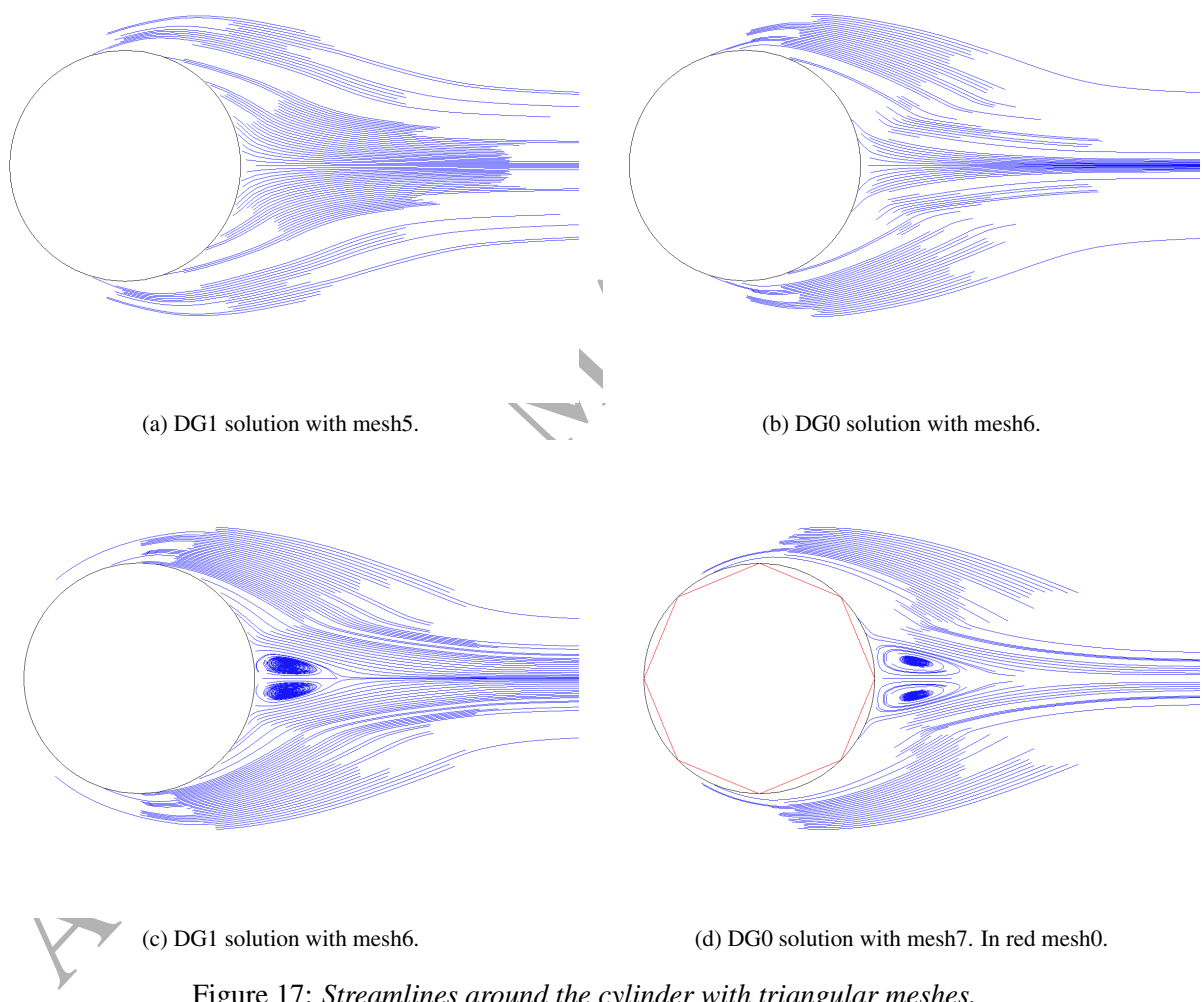


Figure 17: Streamlines around the cylinder with triangular meshes.

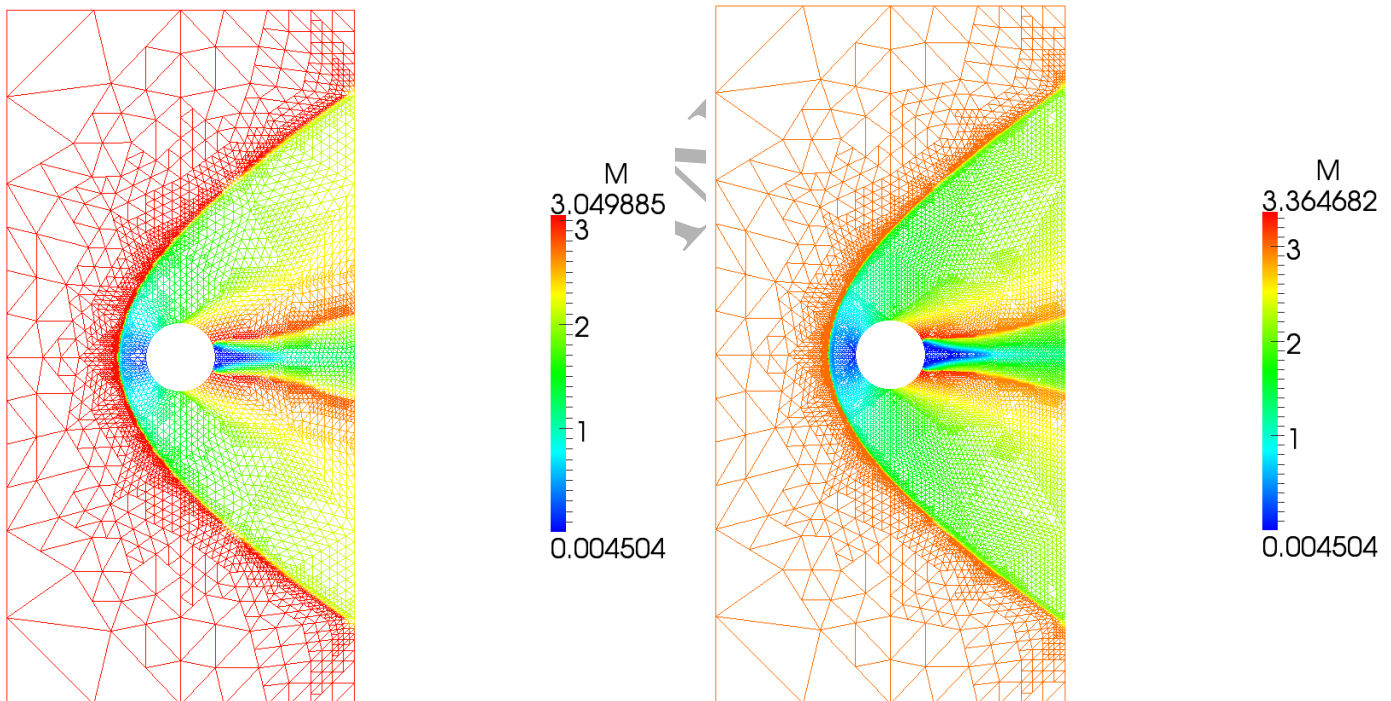


Figure 18: *Mach number isovalues. Left : DG1 solution on mesh6; right : DG0 solution on mesh7.*

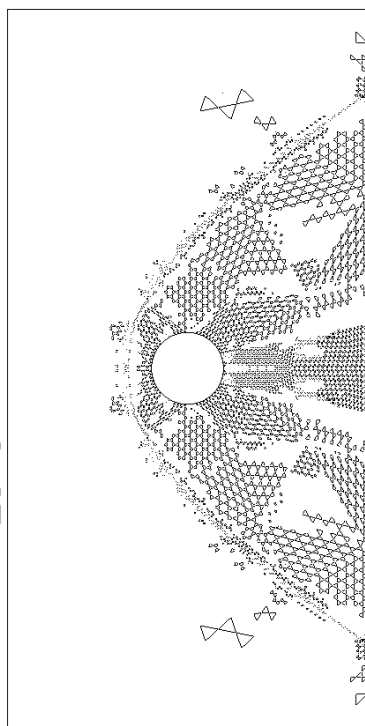


Figure 19: *Refined cells from mesh6 to mesh7 (DG0).*

#### 7.4.2 AHMR procedure on quadrangular meshes: Cylinder test case

This time, the initial quadrangular mesh (figure 16 (a)) has been built ten times finer than the triangular one in the previous sub-section. This choice is done to observe the comportment of the AHMR procedure with a finer mesh from the beginning. In addition, the edges of the quadrangular cells respect some orthogonality properties. Detailed mesh evolution of the AHMR is shown in Table 3 for DG0 and DG1. Because of the fineness of the quadrangular initial mesh, only one and two levels of refinement are needed for DG1 and DG0 respectively to capture (or begin to capture for DG0) the expected vortexes at the rear of the obstacle. Figure 20 shows the meshes at the first (Mesh1) and the second (Mesh2) level of refinement respectively

Table 3: Successive adaptive meshes - Cylinder test case

<b>DG0</b>	<b>Mesh0</b>	<b>Mesh1</b>	<b>Mesh2</b>	<b>Mesh3</b>
Cells	1680	3162	6570	14292
Points	1764	3368	7035	15236
<b>DG1</b>	<b>Mesh0</b>	<b>Mesh1</b>	<b>Mesh2</b>	<b>Mesh3</b>
Cells	1680	3132	6444	13611
Points	1764	3327	6905	14500

Quadrangular meshes with DG0 and DG1.

with DG1 and DG0. The pressure distribution is shown in Figures 21 (a) and (b) for Mesh1 and Mesh2.

The evolutions of streamlines in figure 22 underline the difficulty for DG0 to capture the re-circulation zone even with twice number of cells than DG1 solution. The rarefaction zone is correctly captured at the third level of refinement for the DG0 scheme.

It is not easy task to compare objectively results coming from triangular and quadrangular meshes. Nevertheless, it seems that AHMR with an initial quadrangular mesh finer than triangular one gives a sequence of solutions more accurate even with less mesh points. Indeed, while 27758 and 12128 cells are respectively expected for DG0 and DG1 with triangles (cf. Table 2), only 6570 and 3132 cells are respectively expected for DG0 and DG1 with quadrangles (cf. Table 3) for the same results in term of accuracy. If one compares DG1 solutions, to get similar results only 12528 ( $4 * 3132$ ) degree of freedoms are required with a quadrangular mesh against 36384 ( $3 * 12128$ ) with a triangular mesh. To explain this surprising result, specific studies like the choice of the indicator might be investigated.

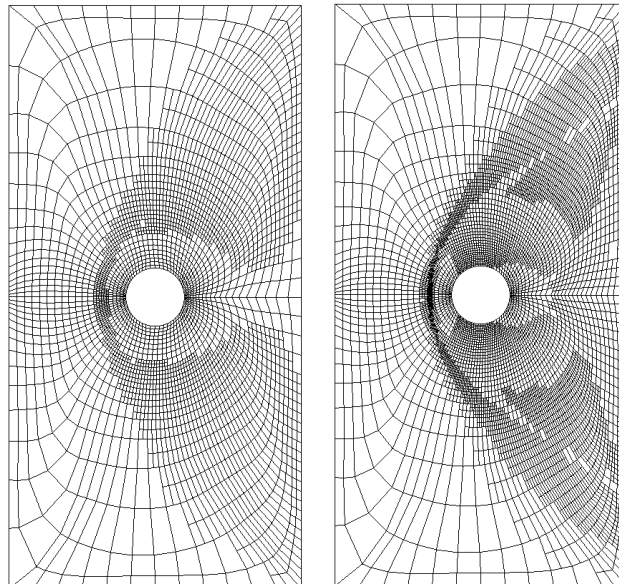


Figure 20: Cylinder test case : meshes obtained at the first level (left) and second level of adaptive refinement for DG1 and DG0 respectively on quadrangular cells.

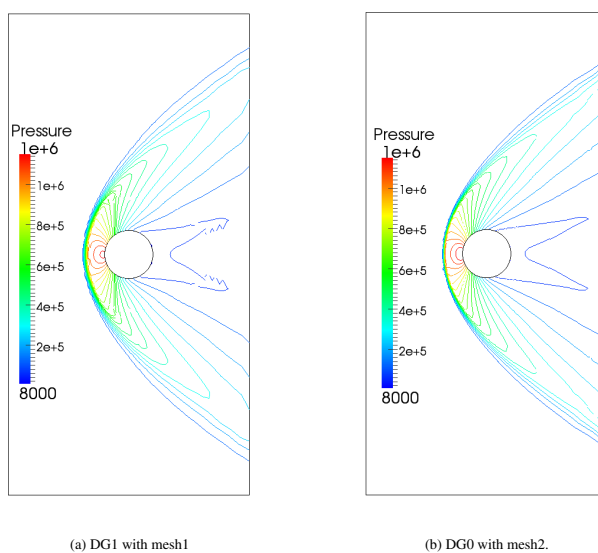
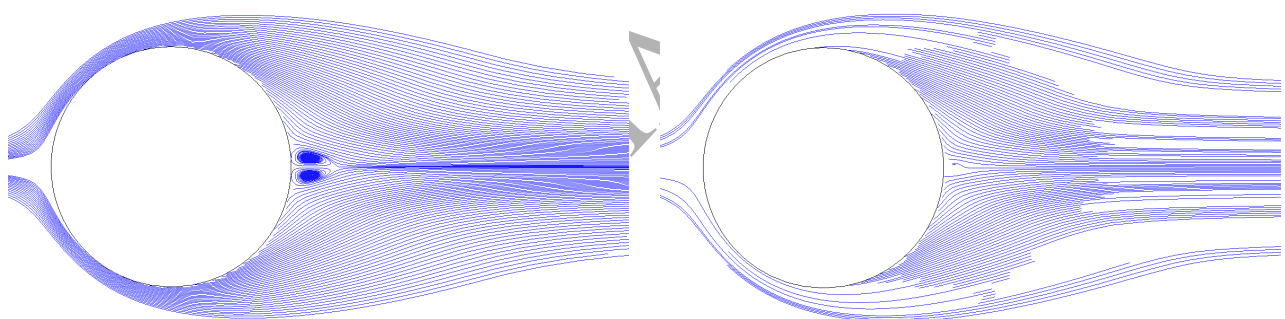


Figure 21: Pressure isovales.



(a) DG1 solution with mesh1.

(b) DG0 solution with mesh2.

Figure 22: *Streamlines around the cylinder with quadrangular meshes*

## 7.5 Supersonic internal flow through a Scramjet with AHMR procedure

This case consists of an internal supersonic flow in a Scramjet inlet at Mach = 3 (see [5] for detailed description of this test case). This test case is very interesting because of the various interactions of different waves between each other and the wall. The error indicator used for the mesh refinement is based on the jump in density at the cell interface [4]. As previously said, triangular and quadrangular meshes are computed using DG0 and DG1 scheme. The initial meshes employed are shown in Figure 23 contain approximatively the same number of cells (1040 for quadrangular and 912 for triangular).

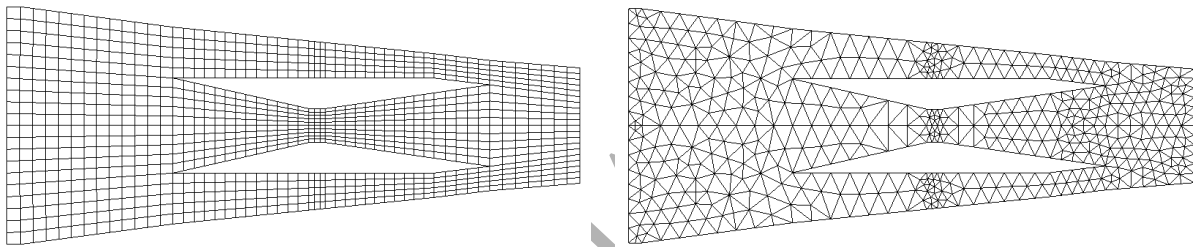


Figure 23: *Initial meshes for the Scramjet test case. Left : quadrangular mesh with 1040 cells; right: triangular mesh with 912 cells.*

### 7.5.1 AHMR procedure on triangular meshes: Scramjet test case

To have an idea of the global mesh evolution with AHMR procedure in both DG0 and DG1 schemes, the final level meshes are presented in Figures 24. The refinement behavior in capturing the multi-scale physical phenomena of the flows in the scramjet inlet is clearly shown. Figure 25 represents the difference between the meshes mesh5 and mesh7 obtained from DG1 and DG0 respectively. This to shows the number of cells roughly to be added to the calculation of DG0 scheme to approximatively obtain the same solution of the calculation of DG1scheme. Although the gradients are slightly more pronounced with DG1, looking at the cutline of the density evolution with DG0 and DG1 in Figure 26, both results look alike. Indeed, these schemes capture as well as the double compression phenomena, the constant density zone between the two shocks and the re-compression in the nozzle extension part of the Scramjet.

Table 4: Successive adaptive meshes - Scramjet test case

<b>DG0</b>	<b>Mesh0</b>	<b>Mesh1</b>	<b>Mesh2</b>	<b>Mesh3</b>	<b>Mesh4</b>	<b>Mesh5</b>	<b>Mesh6</b>	<b>Mesh7</b>
Cells	912	1482	2793	5961	11235	22503	45702	90756
Points	552	933	1723	3540	6459	12708	25727	50549
<b>DG1</b>	<b>Mesh0</b>	<b>Mesh1</b>	<b>Mesh2</b>	<b>Mesh3</b>	<b>Mesh4</b>	<b>Mesh5</b>		
Cells	912	1476	2667	5679	11112	21621		
Points	552	942	1639	3361	6456	12368		

Triangular meshes with DG0 and DG1.

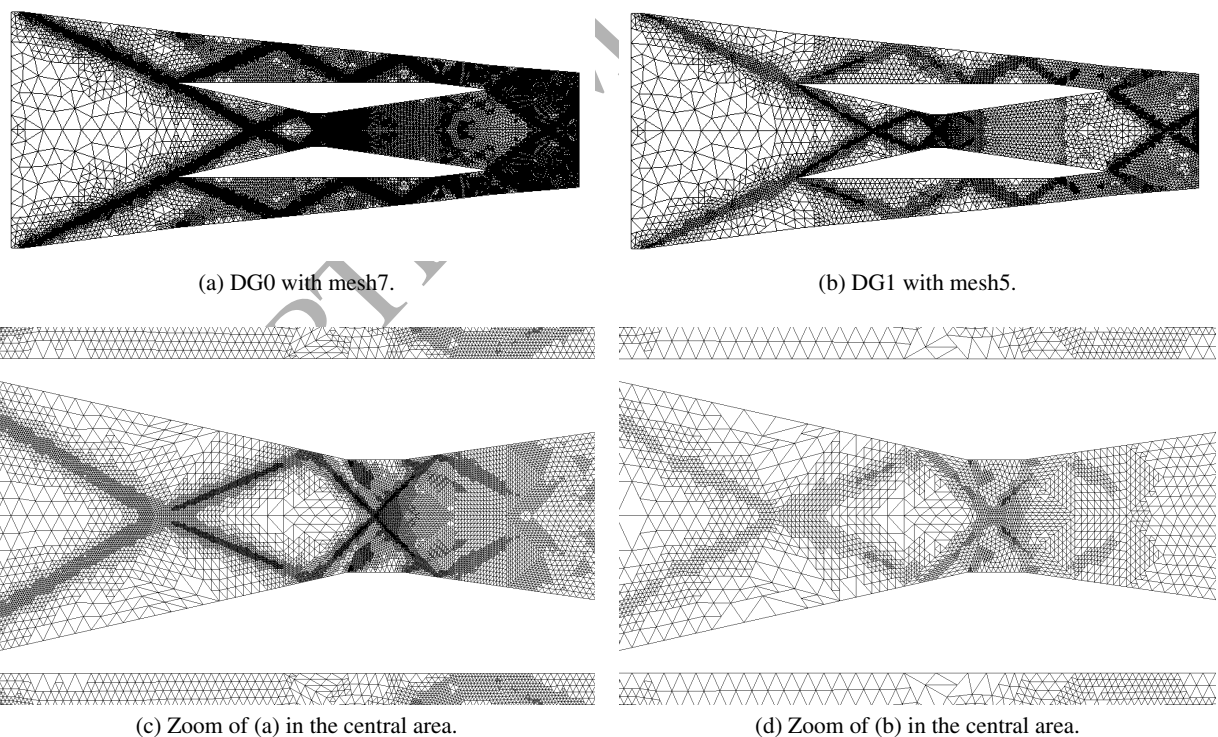


Figure 24: Global and close-up of the observation region view of the adapted meshes for DG0 and DG1 calculations (tri).

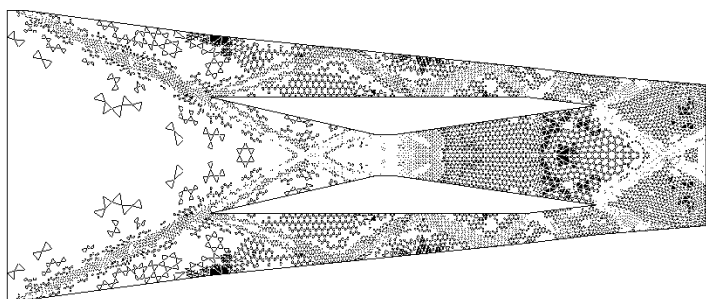


Figure 25: Refined cells from mesh5 with DG1 to mesh7 with DG0 (tri).

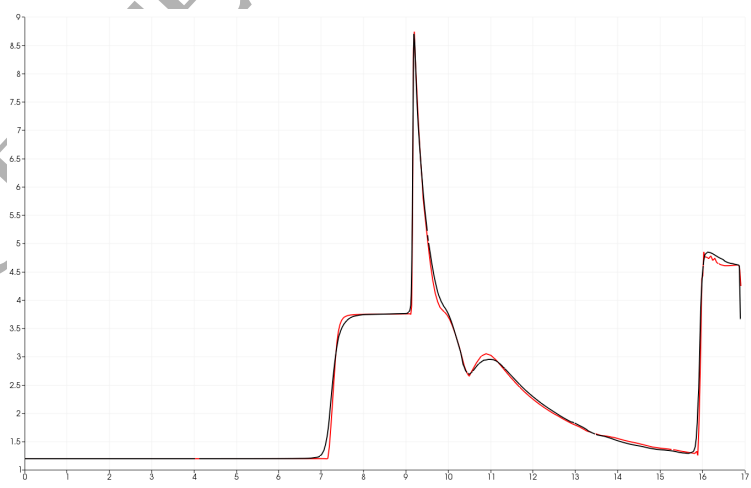


Figure 26: Density cutline along the axis of symmetry - In red DG1-Mesh5 - In black DG0-Mesh7 (tri).

### 7.5.2 AHMR procedure on quadrangular meshes: Scramjet test case

The meshes obtained at the seventh and fifth level of the AHMR process for DG0 and DG1 respectively

Table 5: Successive adaptive meshes - Scramjet test case

<b>DG0</b>	<b>Mesh0</b>	<b>Mesh1</b>	<b>Mesh2</b>	<b>Mesh3</b>	<b>Mesh4</b>	<b>Mesh5</b>	<b>Mesh6</b>	<b>Mesh7</b>
Cells	1040	1994	3674	6782	12824	23708	45074	84653
Points	1175	2284	4151	7571	14219	25768	48774	90948
<b>DG1</b>	<b>Mesh0</b>	<b>Mesh1</b>	<b>Mesh2</b>	<b>Mesh3</b>	<b>Mesh4</b>			
Cells	1040	1769	2747	4361	6518			
Points	1175	2095	3266	5247	7703			

Quadrangular meshes with DG0 and DG1.

contain 84653 and 6518 cells. The axial cutlines of the density in Figure 27 shows the excellent behavior of the DG1 solution from the beginning with Mesh0. Comparing the DG0 solution obtained with the third level mesh DG0 with the DG1 solution on the initial, one can observe the good behavior of the DG1 scheme (see Figure 27-b). In fact the density evolution seem to be more diffusive with the DG0 scheme. Through the isolines of the Mach number field in Figure 30, it can be observed that the DG1 solution (a) seems to depict very well the interactions between the shock-waves and the wall in comparison to the DG0 solution (b) even at the seventh mesh refinement level solution. This tendency is also confirmed when looking at the density cutline of Figure 27. In fact, stronger gradients are notable with the DG1 (red line) than with the DG0 (black line). Furthermore, the maximum value of the density ( $x \sim 9.2$ ) and the re-compression zone ( $x \sim 10.5$ ) phenomenon in the nozzle extension of the Scramjet are more pronounced with the DG1 scheme.

Comparing the results using AHMR between triangular and quadrangular meshes leads to the same conclusion as previously : *Ceteris paribus* in relation to the number of degree of freedom, it is undisputable that the very best result is obtained with quadrangular meshes.

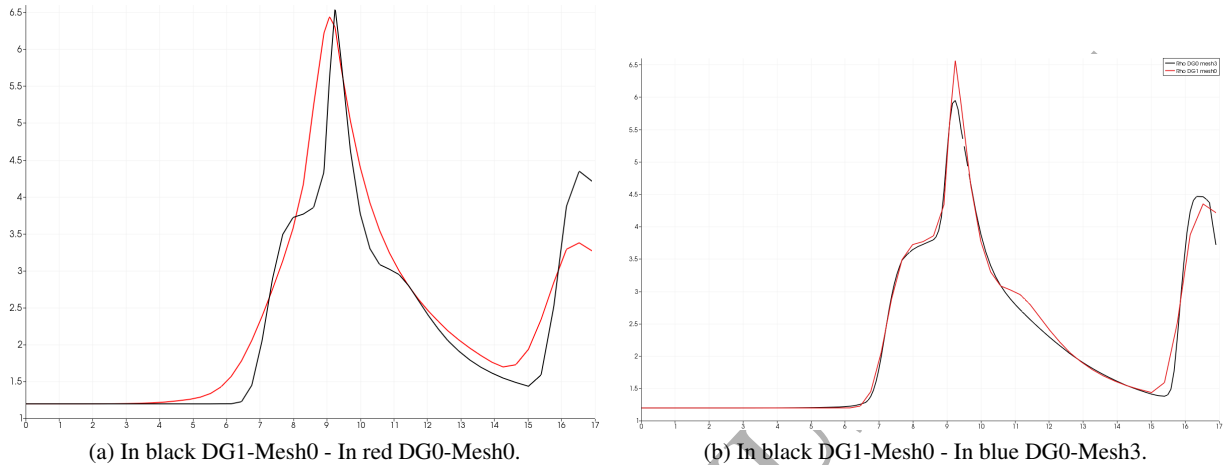


Figure 27: *Density cutline along the axis of symmetry (quad).*

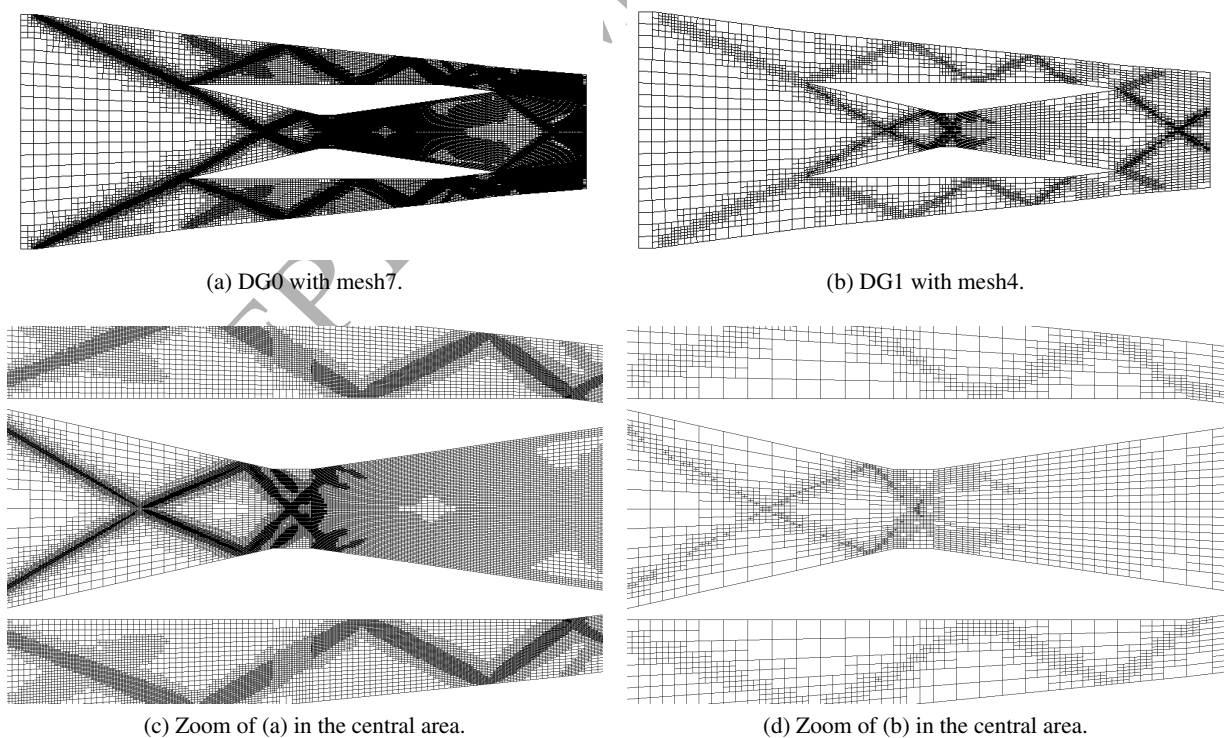


Figure 28: *Global and close-up of the observation region view of the adapted meshes for DG0 and DG1 calculations (quad).*

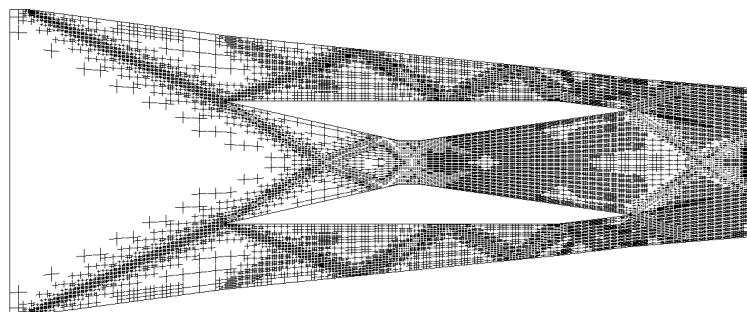
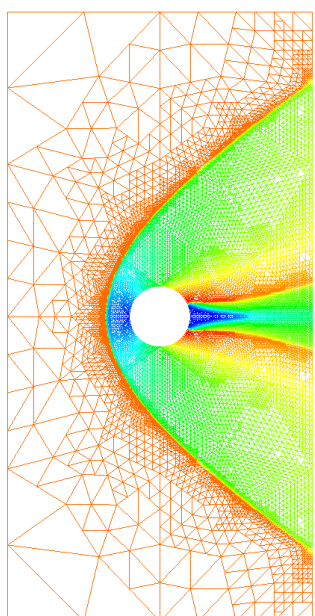
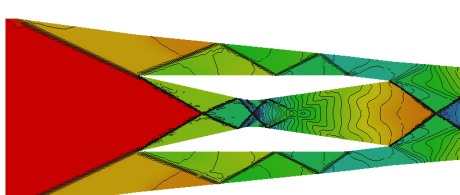
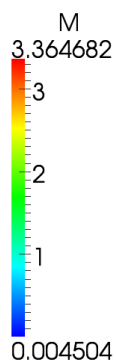


Figure 29: Refined cells from mesh4 with DG1 to mesh7 with DG0 (quad).



(a) DG0 with Mesh7.



(b) DG1 with Mesh4.

Figure 30: Isovalues of Mach number (quad).

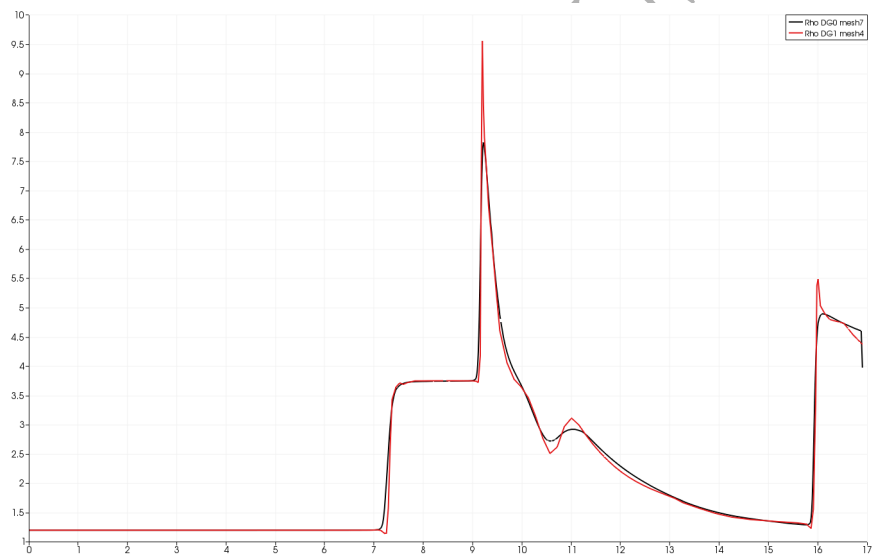


Figure 31: Density cutline along the axis of symmetry - In red DG1-Mesh4 - In black DG0-Mesh7 (quad).

## 8 Conclusion

An efficient higher-order numerical scheme for the solution of the compressible Euler equations has been presented. Several important aspects have been investigated in this paper :

- application of the discontinuous Galerkin method for the space discretization and boundary conditions treatment for curved edges,
- presentation of a limiter for quadrilateral as for triangular meshes suitable for the discontinuous Galerkin method structure's,
- incorporation of the slope limiting procedure into a second order accurate implicit time scheme using DGFEM,
- adaptive mesh refinement with the slope limiting procedure,
- adaptive procedure with hierarchical meshes using hanging-nodes,
- comparison of solutions using triangular and quadrilateral meshes,
- comparison of solutions of DG1 and DG0 schemes during mesh refinement procedure.

The slope limiting procedure method implemented appears to be robust to test cases ranging from transsonic to supersonic flows. The incorporation of the limiting procedure into the implicit time scheme allows to obtain relevant and interesting results in term of accuracy and computational time. So under these conditions and considering the results, a summary of this work can be:

- when comparing DG0 to limited DG1 scheme with the implicit method for transient flow, DG1 gives solutions with more accuracy and efficiency,
- the comparison of this implicit method with explicit Runge-Kutta scheme shows that the Runge-Kutta scheme is much more diffusive for high Mach number flows,
- comparing the numerical solution obtained with AHMR procedure in terms of type of cells on the Cylinder and Scramjet test cases, advantage is given to quadrangular non-conforming meshes. In fact, for the same number of unknowns, solutions obtained with quadrangular cells depict the behavior of the flow with higher accuracy and with more efficiency. In one of our previous papers [5] it has been shown that the result is the opposite with DG0.

Taking into consideration all these results some perspectives and directions can be expressed as :

- extend the limiting process to any high order elements in *hp-typed* mesh adaptation,
- evaluate rigorously the advantage-disadvantage of the spending CPU time and the cost of the storage memory as far as the order increases with DGFEM,
- compare several types of criterion of mesh refinement on triangular and quadrangular grids,
- improve the AHMR procedure to investigate adjoint-based mesh refinement.

Numerical simulation in engineering sciences is very open because of the important number of parameters which can be used and which can significantly impact. Efficiency, accuracy and robustness, the famous *Triptych* of numerical simulation depends here again on the choice of the AHMR procedure, the geometry of the element and the time scheme. Furthermore this list is not exhaustive.

## Funding Acknowledgement

Part of this research is supported by public finance of the "Direction Générale de la Compétitivité de l'Industrie et des Services" (D.G.C.I.S.) through the OPTIMAL research program, recognized by the three French aeronautical poles of competitiveness (Aerospace Valley, ASTech Paris-Area and Pôle PEGASE). We express our gratitude to the *Concha* team and especially to Roland Becker and David Trujillo for their help in the development of the Concha Library.

## References

- [1] S. Aliabadi and T. Tezduyar. Space-time finite element computation of compressible flows involving moving boundaries and interfaces. *Comput. Methods Appl. Mech. Eng.*, 107:209–223, 1993.
- [2] F. Bassi and S. Rebay. A high-order accurate discontinuous finite element method for the numerical solution of the compressible navier-stokes equations. *Journal of computational physics*, 131:267–279, 1997.
- [3] F. Bassi and S. Rebay. High-order accurate discontinuous solution of the 2d euler equations. *Journal of computational physics*, 138:251–285, 1997.
- [4] R. Becker, K. Gokpi, E. Schall, and D. Trujillo. Comparison of two types of a posteriori error estimators on mesh adaptation in discontinuous galerkin finite elements methods. *Journal of Aerospace Engineering*, 2:222 – 239, 2012.
- [5] R. Becker, K. Gokpi, E. Schall, and D. Trujillo. Fully implicit adaptive method using discontinuous galerkin finite elements for high speed flows. *Int. J. Aerodynamics*, 2:222 – 239, 2012.
- [6] R. Becker and D. Trujillo. Concepts of the finite element library concha. Tenth International Conference Zaragoza-Pau on Applied Mathematics and Statistics, Monogr. Semin. Mat. Garcia Galdeano, Prensas Univ. Zaragoza, Zaragoza, 2011.
- [7] B. Cockburn. Devising discontinuous galerkin methods for non-linear hyperbolic conservation laws. *Journal of computational and applied mathematics*, 128:187–204, 2001.

- [8] B. Cockburn, S. Hou, and C. W. Shu. Tyb runge-kutta local projection discontinuous galerkin finite element method for conservation laws iv: The multidimensional case. *Math. Comp.*, 54:545–581, 1990.
- [9] B. Cockburn and C.-W. Shu. Runge-kutta discontinuous galerkin methods for convection-dominated problems. *SIAM J. Sci. Comput.*, 16:173–261, 2001.
- [10] N. T. Frink. Assessment of an unstructured grid method for predicting 3d turbulent viscous flow. AIAA paper 96-0292.
- [11] R. Hartmann. The role of the jacobian in the adaptive discontinuous galerkin method for the compressible euler equations. In G. Warnecke, editor, *Analysis and Numerics for Conservation Laws*, pages 301–316. Springer Berlin Heidelberg, 2005.
- [12] J. Hesthaven and T. Warburton. *Nodal Discontinuous Galerkin Methods: Algorithms, Analysis, and Applications*. Texts in Applied Mathematics, Springer, 2008.
- [13] P. Jawahar and H. Kamath. A high-resolution procedure for euler and navier-stokes computations on unstructured grids. *Journal of computational physics*, 164:165–203, 2000.
- [14] A. Klöckner, T. Warburton, and J. S. Hesthaven. Viscous shock capturing in a time-explicit discontinuous galerkin method. *Mathematical Modelling of Natural Phenomena*, 6:57–84, 2011.
- [15] L. Krivodonova and M. Berger. High-order accurate implementation of solid wall boundary conditions in curved geometries. *Journal of computational physics*, 211:492–512, 2006.
- [16] A. Loseille, A. Dervieux, and F. Alauzet. Fully anisotropic goal-oriented mesh adaptation for 3d steady Euler equations. *Journal of computational physics*, 229(8):2866–2897, 2010.
- [17] H. Luo, J. D. Baum, and R. Lohner. A p-multigrid discontinuous galerkin method for the euler equations on unstructured grids. *Journal of computational physics*, 211:767–783, 2006.

- [18] P. Lyra and K. Morgan. A review and comparative study of upwind biased schemes for compressible flow computation. part iii: Multidimensional extension on unstructured grids. *Archives of Computational Methods in Engineering*, 9:207–256, 2002.
- [19] D. Mavriplis, N. C., K. Shahbazi, L. Wang, and N. Burgess. Progress high-order discontinuous galerkin methods for aerospace applications. *AIAA Aerospace Sciences Meeting Including The New Horizons Forum and Aerospace Exposition*, 601, 2009.
- [20] P.-O. Persson and J. Peraire. Sub-cell shock capturing for discontinuous galerkin methods. In Proc. of the 44th AIAA Aerospace Sciences Meeting and Exhibit, 2006.
- [21] E. F. Toro. *Riemann Solvers and Numerical Methods for Fluid Dynamics*. Springer-Verlag, 1997.
- [22] S. Tu and S. Aliabadi. A slope limiting procedure in discontinuous galerkin finite element method for gasdynamic applications. *Int. J. Numer. Anal. Model.*, 2:163–178, 2005.
- [23] V. Venkatakrishnan. Convergence to steady solutions of the euler equations on unstructured grids with limiters. *Journal of computational physics*, 118:120–130, 1995.
- [24] L. Wang and D. J. Mavriplis. Implicit solution of the unsteady euler equations for high-order accurate discontinuous galerkin discretizations. *Journal of computational physics*, 225(2):1994 – 2015, 2007.